J. Fluid Mech. (1996), *vol.* 306, *pp.* 83–109

Penetration of a blade into a vortex core: vorticity response and unsteady blade forces

By J. S. MARSHALL[1] AND J. R. GRANT[2]

[1] Department of Mechanical Engineering and Iowa Institute of Hydraulic Research,
The University of Iowa, Iowa City, IA 52242, USA

[2] Naval Undersea Warfare Center, Building 1302, Newport, RI 02841, USA

(Received 31 May 1994 and in revised form 26 July 1995)

Numerical calculations are performed for the problem of penetration into a vortex core of a blade travelling normal to the vortex axis, where the plane formed by the blade span and the direction of blade motion coincides with the normal plane of the vortex axis at the point of penetration. The calculations are based on a computational method, applicable for unsteady three-dimensional flow past immersed bodies, in which a *collocation* solution of the vorticity transport equation is obtained on a set of Lagrangian control points. Differences between this method and other Lagrangian vorticity-based methods in the literature are discussed. Lagrangian methods of this type are particularly attractive for problems of unsteady vortex–body interaction, since control points need only be placed on the surface of the body and in regions of the flow with non-negligible vorticity magnitude. The computations for normal blade–vortex interaction (BVI) are performed for an inviscid fluid and focus on the relationship between the vortex core deformation due to penetration of the blade into the vortex ambient position and the resulting unsteady pressure field and unsteady force acting on the blade. Computations for cases with different vortex circulations are performed, and the accuracy of an approximate formulation using rapid distortion theory is assessed by comparison with the full computational results for unsteady blade force. The force generated from blade penetration into the vortex ambient position is found to be of a comparable magnitude to various other types of unsteady BVI forces, such as that due to cutting of the vortex axial flow.

1. Introduction

The current paper is concerned with the vorticity response and unsteady blade forces which occur as a blade moves through the ambient position occupied by a vortex core in an inviscid fluid, where the plane formed by the blade span and the direction of blade forward velocity coincides with the normal plane of the vortex axis. We will henceforth refer to the blade–vortex interaction in this geometry as *normal BVI*, and say that the blade *penetrates* into the vortex core, it being understood that the vortex will deform about the blade and the vortex lines will not be severed by the blade in an inviscid fluid. Normal BVI occurs in a number of rotorcraft aerodynamical problems, such as interaction of trailing tip vortices from a helicopter main rotor blade with the tail section or with blades from the tail rotor and entrainment of atmospheric turbulence or shed vortices into helicopter rotors. Other applications include interaction between ship propellers and coherent structures in the ship boundary layer and ingestion of atmospheric turbulence into jet engine fans.

When normal BVI does occur, it may emit an impulsive noise which sometimes dominates the sound generation of the device (see, for example, a study of noise generation from Lynx helicopters by Leverton, Pollard & Wills 1977). Theoretical models of the sound generation by normal BVI have been developed by Amiet (1986), Amiet, Simonich & Schlinker (1990) and Howe (1988, 1989). These studies typically either prescribe the vortex response to cutting or make other idealizations to simplify the analysis. Common idealizations are restriction to circular vortex core cross-section and the assumption that the vortex is convected only by the ambient flow about the blade. Controlled experimental studies of noise generation by normal BVI have been performed by Ahmadi (1986), Cary (1987) and Schlinker & Amiet (1983). Some of these studies also report limited flow visualization results (using smoke in a wind tunnel); however, the details of the deformation of the vorticity field near the blade leading edge are not clear.

An experimental study of the fluid dynamical aspects of normal BVI was reported by Johnston & Sullivan (1992) in which the trailing vortex from a propeller was cut by a blade traversed from downstream. The vortex deformation due to cutting by the blade was visualized by smoke, and the unsteady pressure field on the blade surface was measured. For blades at an angle of attack of 5° or more, the two parts of the vortex were shown to undergo spanwise displacements (in opposite directions) after being cut by the blade. It was also noted that the presence of axial flow within the core causes a thickening of the vortex core on one side of the blade and a thinning on the other side following cutting.

Another experimental study of normal BVI was performed by Weigand (1993) in an investigation of the response of a vortex ring to a cut normal to the core axis by a thin flat plate. This study was performed in water, and used dye to visualize the vortex and particle-image velocimetry to measure the axial flow within the vortex core. Weigand observed that cutting of the vortex by the plate causes the formation of a 'sloshing' type wave on the ring in which the core area varies (nearly) periodically at any given point along the vortex axis. Secondary vortices are formed by vortex-induced separation of the blade boundary layer, which interact with the primary ring vortex. In some such cases, the secondary–primary vortex interaction results in breakup of the ring and formation of three individual vortex rings propagating orthogonally to each other.

A recent theoretical and computational study dealing with the problem of cutting of a line vortex by a blade at angle of attack α and with finite thickness T is reported in Marshall (1994) and Marshall & Yalamanchili (1994). In Marshall (1994), a general long-wave approximation of the theory of vortex filaments with variable core area is developed as a simplification of the vortex filament theories of Lundgren & Ashurst (1989) and Marshall (1991), which applies to problems where the axial lengthscale L of the vortex disturbance is large compared to the core radius. An analytical solution of the long-wave theory is obtained in Marshall (1994) for the response of a straight vortex (with ambient axial velocity w_0 and core radius σ_0) to instantaneous cutting by a thin flat plate (with forward speed U relative to the vortex and angle of attack α). The solution predicts propagation of a 'vortex shock' (over which the core radius changes discontinuously) and a 'vortex expansion wave' away from the blade on opposite sides of the vortex. The subsequent difference in vortex core radius across the blade results in an impulsive normal force on the blade surface.

The possibility of bending of the vortex due to interaction with thick blades is investigated in Marshall & Yalamanchili (1994) with numerical computations based on the long-wave vortex filament model. The cutting of the vortex by the blade is again assumed to occur instantaneously when the blade leading edge penetrates sufficiently far into the vortex core. It is found that the vortex will remain nearly straight during passage of the blade for ratios T/σ_0 of blade thickness to ambient core radius of order unity or less; however, for T/σ_0 greater than about 5 considerable bending of the vortex about the blade leading edge is observed to occur. For sufficiently large T/σ_0 values, the vortex bends so much that the blade leading edge never cuts the vortex, but rather the vortex impinges on each side of the blade surface at points somewhat downstream of the leading edge. The main results of Marshall (1994) and Marshall & Yalamanchili (1994) have also been confirmed experimentally (Krishnamoorthy 1993; Krishnamoorthy & Marshall 1994).

In the present paper, the results of a direct numerical computation of the penetration of a blade into a vortex core in an inviscid fluid is reported. The neglect of viscous effects in these computations can be partially justified via a scaling analysis, for the purpose of computing the unsteady blade force, for cases where the maximum azimuthal speed induced by the vortex is of the same order as the blade forward speed and the blade thickness is of the same order as the vortex core radius. The numerical calculations are performed using a *collocation* solution of the vorticity transport equation on a set of convected (or Lagrangian) control points. The method utilizes a representation for the vorticity field as a set of overlapping elements, similar to the 'vortex blob' method (e.g. Knio & Ghoniem 1990; Winckelmans & Leonard 1993), which converges to the prescribed vorticity field as the number of control points becomes large (with fixed element overlap). Most vortex methods in the literature (e.g. Anderson & Greengard 1985; Beale & Majda 1982; Leonard 1985) associate some constant volume h^3 with each control point, where the product $h^3\boldsymbol{\omega}_n$ of this volume with the vorticity evaluated at the control point is the integral over space of all vorticity associated with element n (which we refer to as the element 'amplitude' $\boldsymbol{\Omega}_n$). Since h^3 is constant in time and the evolution of $\boldsymbol{\omega}_n$ is governed by the usual vorticity transport equation, this approach is equivalent to writing a transport equation for $\boldsymbol{\Omega}_n$ of a form analogous to that for vorticity (as noted by Winckelmans & Leonard 1993). In the present collocation method, the element amplitudes are instead obtained by fitting the element representation to the vorticity values at the control points, which for N control points involves solution of an $N \times N$ matrix equation at each time step. We use an approximate iterative procedure for solution of this matrix equation, which both greatly speeds up the calculation and filters out noise in the solution for element amplitudes due to ill-conditioning of the matrix. A method for collocation solution of the vorticity transport equation in two dimensions was previously introduced by Beale (1986), and later employed by Choquin & Lucquin-Desreux (1988); however, some differences exist between our method and that of Beale (1986) in the procedure used to fit the element amplitudes (see §2). The Lagrangian collocation method used here has also been extended to viscous flows and to flows with background vorticity fields; these will be described in a separate paper along with more technical details of the numerical analysis.

A description of the algorithm used for the numerical computation of the vorticity evolution is given in §2. Several diagnostic tests of the numerical method are described in §3. Details of the implementation of the numerical method for the normal BVI problem are described in §4. The results of computations for the deformation of the vorticity field in the normal BVI problem during penetration of a blade into a vortex are described in §5, along with an assessment of the accuracy of the numerical calculations. In §6, the unsteady pressure on the blade is calculated using an integral equation formulation of the pressure-Poisson equation. The results for unsteady blade force are compared for different vortex circulations in §7. The applicability of rapid-distortion theory to the normal BVI problem, which has been used in previous treatments of acoustic aspects of the problem, is also evaluated in §§ 5–7 in comparison to the results for the full inviscid calculation.

2. Numerical method

A method is described in this section for solution of three-dimensional unsteady flows which is based on a collocation solution of the vorticity transport equation on a set of N convected control points. In this method, the evolution of the vorticity vector $\boldsymbol{\omega} = \nabla \times \boldsymbol{u}$ is determined from the inviscid vorticity transport equation

$$\frac{\mathrm{d}\boldsymbol{\omega}}{\mathrm{d}t} = (\boldsymbol{\omega}\cdot\nabla)\boldsymbol{u}, \tag{1}$$

where $\mathrm{d}/\mathrm{d}t$ is the material derivative and $\boldsymbol{u}$ is the velocity vector. The velocity field is obtained by integration over the vorticity in the Biot–Savart equation

$$\boldsymbol{u}(\boldsymbol{x},t) = \boldsymbol{v}(\boldsymbol{x},t) - \frac{1}{4\pi}\int_V \frac{\boldsymbol{r}\times\boldsymbol{\omega}(\boldsymbol{x}',t)}{r^3}\,\mathrm{d}v(\boldsymbol{x}'). \tag{2}$$

In (2), we define $\boldsymbol{r} = \boldsymbol{x}-\boldsymbol{x}'$ and $r = |\boldsymbol{r}|$, and let V denote the entire space occupied by the fluid and $\mathrm{d}v(\boldsymbol{x}')$ denote an infinitesimal volume element in V, where the integration is with respect to the primed position vector $\boldsymbol{x}'$. The vector $\boldsymbol{v}(\boldsymbol{x},t)$ is a potential flow field determined by the boundary conditions on $\boldsymbol{u}$.

The vorticity vector $\boldsymbol{\omega}$ can be decomposed as the sum of a divergent vector field, which we refer to as the 'generator' field $\boldsymbol{q}(\boldsymbol{x},t)$, and the gradient of a scalar, such that

$$\boldsymbol{\omega} = \boldsymbol{q} - \nabla\alpha. \tag{3}$$

As noted both by Novikov (1983) and Winckelmans & Leonard (1993), the gradient term in (3) makes no contribution to the induced velocity from (2). The curl of $\boldsymbol{q}$ is equal to the curl of $\boldsymbol{\omega}$, and the divergence of $\boldsymbol{q}$ is obtained from (3) as

$$\nabla\cdot\boldsymbol{q} = \nabla^2\alpha. \tag{4}$$

Substituting (3) into (2), taking the curl of $\boldsymbol{u}$, and using some standard vector identities and the fact that $\nabla^2(1/r) = -4\pi\delta(r)$, an expression for the vorticity in terms of $\boldsymbol{q}$ is obtained as (see also Winckelmans & Leonard 1993)

$$\boldsymbol{\omega}(\boldsymbol{x},t) = \boldsymbol{q}(\boldsymbol{x},t) - \nabla\left[\frac{1}{4\pi}\int_V \frac{\boldsymbol{q}(\boldsymbol{x}',t)\cdot\boldsymbol{r}}{r^3}\,\mathrm{d}v(\boldsymbol{x}')\right]. \tag{5}$$

In order to evaluate the integral in (2) to obtain the velocity field, a representation for the generator field in terms of overlapping elements, centred at the control points $\boldsymbol{x}_n(t)$, $n = 1,\ldots,N$, is introduced as

$$\boldsymbol{q}(\boldsymbol{x},t) = \sum_{n=1}^{N} \boldsymbol{\Omega}_n(t) f_n(\boldsymbol{x}-\boldsymbol{x}_n(t), R_n(t)), \tag{6}$$

where $\boldsymbol{x}$ is any arbitrary point in V. The vectors $\boldsymbol{\Omega}_n(t)$ are called the element 'amplitudes' and are equal to the total (integrated) vorticity associated with each element. The scalars f_n are called the element 'weighting functions' (not to be confused with 'weight functions' in finite-element methods) and are normalized such that

$$\int_V f_n(\boldsymbol{x}-\boldsymbol{x}_n(t), R_n(t))\,\mathrm{d}v = 1. \tag{7}$$

The weighting functions determine the distribution of vorticity within each element. The function $R_n(t)$ is a lengthscale associated with the element weighting function, called the element 'radius'. In general, there may be several lengthscales associated with the weighting function, but for the present paper we consider only weighting functions with a single radius in the Gaussian form

$$f_n(\boldsymbol{x}-\boldsymbol{x}_n, R_n) = \frac{1}{\pi^{3/2}R_n^3}\exp(-|\boldsymbol{x}-\boldsymbol{x}_n|^2/R_n^2). \tag{8}$$

Substituting (6) and (8) into the Biot-Savart equation (2) and performing the integration, the velocity at any point $\boldsymbol{x}$ in the flow field is obtained as

$$\boldsymbol{u}(\boldsymbol{x},t) = \boldsymbol{v}(\boldsymbol{x},t)+\sum_{n=1}^{N}\frac{P(\frac{3}{2},|\boldsymbol{x}-\boldsymbol{x}_n|^2/R_n^2)}{4\pi|\boldsymbol{x}-\boldsymbol{x}_n|^3}\boldsymbol{\Omega}_n\times(\boldsymbol{x}-\boldsymbol{x}_n), \tag{9}$$

where $P(a,z)$ is the incomplete gamma function with limits $P=0$ at $z=0$ and $P=1$ as $z\rightarrow\infty$. When $a=3/2$ and $z=x^2$, for some real variable x, a convenient expression for $P(3/2,x^2)$ is given in terms of the error function erf (x) as (Abramowitz & Stegun 1965)

$$P(\tfrac{3}{2},x^2) = \operatorname{erf}(x)-\frac{2x\,\mathrm{e}^{-x^2}}{\pi^{1/2}}. \tag{10}$$

Substituting (6) and (8) into (5) gives the vorticity field as

$$\boldsymbol{\omega}(\boldsymbol{x},t) = \sum_{n=1}^{N}\left\{\frac{\boldsymbol{\Omega}_n}{\pi^{3/2}R_n^3}\exp\left(-\frac{|\boldsymbol{x}-\boldsymbol{x}_n|^2}{R_n^2}\right)-\nabla\left[\frac{P(\frac{3}{2},|\boldsymbol{x}-\boldsymbol{x}_n|^2/R_n^2)}{4\pi|\boldsymbol{x}-\boldsymbol{x}_n|^3}\boldsymbol{\Omega}_n\cdot(\boldsymbol{x}-\boldsymbol{x}_n)\right]\right\}. \tag{11}$$

Since the vorticity in (11) is constructed using (5), it is divergence-free for any weighting function f_n. From (11) a matrix equation for the element amplitudes $\boldsymbol{\Omega}_n$ can be written as

$$\boldsymbol{\omega}_m = \sum_{n=1}^{N}\left\{W_{mn}\boldsymbol{\Omega}_n - A_{mn}\frac{\boldsymbol{x}_m-\boldsymbol{x}_n}{|\boldsymbol{x}_m-\boldsymbol{x}_n|^2}[\boldsymbol{\Omega}_n\cdot(\boldsymbol{x}_m-\boldsymbol{x}_n)]\right\}, \tag{12}$$

where $\boldsymbol{\omega}_m$ denotes the values of vorticity at the control points $\boldsymbol{x}_m$, and W_{mn} and A_{mn} are $N\times N$ time-dependent matrices defined by

$$\left.\begin{aligned} W_{mn} &= \frac{1}{\pi^{3/2}R_n^3}\exp\left(-\frac{|\boldsymbol{x}_m-\boldsymbol{x}_n|^2}{R_n^2}\right)-\frac{1}{4\pi|\boldsymbol{x}_m-\boldsymbol{x}_n|^3}P(\tfrac{3}{2},|\boldsymbol{x}_m-\boldsymbol{x}_n|^2/R_n^2),\\ A_{mn} &= \frac{1}{\pi^{3/2}R_n^3}\exp\left(-\frac{|\boldsymbol{x}_m-\boldsymbol{x}_n|^2}{R_n^2}\right)-\frac{3}{4\pi|\boldsymbol{x}_m-\boldsymbol{x}_n|^3}P(\tfrac{3}{2},|\boldsymbol{x}_m-\boldsymbol{x}_n|^2/R_n^2). \end{aligned}\right\} \tag{13}$$

The algorithm described above is essentially a means of interpolating the vorticity field given its values on a set of irregularly spaced control points, with the integral (2) produced by analytically performing the indicated integration on the individual interpolating functions. Similar methods can be used generally for interpolation of fields specified on irregularly spaced points and for evaluating integrals over these fields. Indeed, we will use such a method in performing the volume integration in (24) below.

In the context of a general interpolation formula, we ask that the weighting function f_n in (6) be of significant magnitude only in a region of scale R and that f_n be doubly differentiable. In order that the same fit yield a simple expression for the Biot-Savart integral of the quantity, we further ask that the integral (2) be obtainable analytically (or nearly so) over the terms of the sum (6). There is a large class of spherically symmetric functions that meet these requirements, in addition to the Gaussian used here (see, for example, Winckelmans & Leonard 1993).

In computing the evolution of the flow, we initially prescribe some vorticity field $\boldsymbol{\omega}$, solve the matrix equation (12) for the element amplitudes $\boldsymbol{\Omega}_n$ and then solve for the velocity at each control point using the sum (9). The potential velocity field $\boldsymbol{v}$ in (9) is necessary to enforce the no-penetration boundary condition on the surface of immersed bodies and is solved for using a combination of source and vortex sheet panel methods (Hess & Smith 1967; Uhlman & Grant 1993). The flow field at the next time step is obtained by convecting the control points according to

$$\frac{\mathrm{d}\boldsymbol{x}_n}{\mathrm{d}t} = \boldsymbol{u}(\boldsymbol{x}_n, t) \tag{14}$$

and then solving for the change in vorticity at each control point from (1). The stretching term in (1) is obtained in the present study by the centred finite-difference approximation

$$(\boldsymbol{\omega}\cdot\nabla)\,\boldsymbol{u}\,|_{x_m} = \frac{\omega}{2\Delta x}[\boldsymbol{u}(\boldsymbol{x}_m + \boldsymbol{a}\,\Delta x) - \boldsymbol{u}(\boldsymbol{x}_m - \boldsymbol{a}\,\Delta x)], \tag{15}$$

where ω is the magnitude of $\boldsymbol{\omega}$, $\boldsymbol{a} = \boldsymbol{\omega}/\omega$ is the direction of $\boldsymbol{\omega}$ and the increment Δx can be made arbitrarily small. We could alternatively have obtained the stretching term by taking the gradient of $\boldsymbol{u}$ using the result (9), but the finite-difference approximation (15) considerably speeds up the calculation.

Once $\boldsymbol{\omega}$ is known at the control points at the new time step, the amplitudes $\boldsymbol{\Omega}_n$ are again obtained from (12) and the process is repeated. In the current work, a second-order predictor–corrector scheme was used to advance the calculation in time in order to ensure stability and second-order accuracy of the numerical method. Letting $\boldsymbol{R}$ denote the right-hand side of (1) and an asterisk denote evaluate at the end of the predictor step, the predictor–correct scheme used to advance the solution in time can be expressed as

$$\frac{\boldsymbol{\omega}_k^* - \boldsymbol{\omega}_k^n}{\Delta t} = \boldsymbol{R}_k^n, \quad \frac{\boldsymbol{\omega}_k^{n+1} - \boldsymbol{\omega}_k^n}{\Delta t} = \tfrac{1}{2}(\boldsymbol{R}_k^n + \boldsymbol{R}_k^*), \tag{16a, b}$$

where $\boldsymbol{\omega}_k^n = \boldsymbol{\omega}(\boldsymbol{x}_k, t_n)$ and $\boldsymbol{R}_k^n = \boldsymbol{R}(\boldsymbol{x}_k, t_n)$.

One difficulty with the algorithm described above is that direct inversion of the matrix equation (12) to obtain $\boldsymbol{\Omega}_n$ requires a large amount of computational time when large numbers of elements are present. Also, when elements overlap by substantial amounts, which is necessary in order to maintain a smooth representation of the vorticity field in (11), the resulting matrix equation for $\boldsymbol{\Omega}_n$ is ill-conditioned, such that an exact solution of (12) for a fairly smooth vorticity field yields $\boldsymbol{\Omega}_n$ values with large oscillations between nearby points. Both of these problems can be overcome by using an iterative scheme in which $\boldsymbol{\Omega}_n$ is temporarily assumed to remain constant for elements with n in some set $Q(m)$, where m is the index for the control point at which the solution is desired, and control points $\boldsymbol{x}_n$ with index n in $Q(m)$ lie in some small region surrounding $\boldsymbol{x}_m$. Letting $P(m)$ denote the complement of $Q(m)$, an iteration formula for the element amplitude is obtained as

$$\begin{aligned}\boldsymbol{\omega}(\boldsymbol{x}_m, t) = &\sum_{n\in Q(m)} \left\{ W_{mn}\boldsymbol{\Omega}_m^{(q+1)} - A_{mn}\frac{\boldsymbol{x}_m - \boldsymbol{x}_n}{|\boldsymbol{x}_m - \boldsymbol{x}_n|^2}[\boldsymbol{\Omega}_m^{(q+1)}\cdot(\boldsymbol{x}_m - \boldsymbol{x}_n)]\right\} \\ &+ \sum_{n\in P(m)} \left\{ W_{mn}\boldsymbol{\Omega}_n^{(q)} - A_{mn}\frac{\boldsymbol{x}_m - \boldsymbol{x}_n}{|\boldsymbol{x}_m - \boldsymbol{x}_n|^2}[\boldsymbol{\Omega}_n^{(q)}\cdot(\boldsymbol{x}_m - \boldsymbol{x}_n)]\right\},\end{aligned} \tag{17}$$

where q is the iteration index.

It is noted that the iterative scheme (17) does not converge to an exact solution of (12), but instead converges to a smooth fit for the amplitudes $\boldsymbol{\Omega}_n$ with vorticity error at any point of order $l^2\nabla^2\omega$, where l is a typical separation distance between neighbouring control points. The representation becomes more accurate as the resolution of the vorticity field by the element control points improves. Exact iteration procedures, such as that of Beale (1986), exhibit the same type of 'noisy' behaviour as the exact solution of (12) after a sufficient number of iterations. A related discussion of the trade-off between accuracy and smoothness in solution of inverse problems is given in the book by Press *et al.* (1992, pp. 795–799). The approximate iteration procedure (17) is similar to the 'function specification method' commonly used to obtain approximate solutions of the inverse heat conduction problem (Beck, Blackwell & St. Clair 1985). Diagnostic tests with this iteration scheme have been performed in one dimension using temperature profiles of various forms, in two dimensions with vortex patches and in three dimensions with vortex rings.The iteration scheme seems to be quite robust and usually converges (with a maximum relative change in $\boldsymbol{\Omega}_n$ of less than 10^{-6}) in 6–10 iterations. In two-dimensional tests with vortex patches, the typical error in vorticity (normalized by the vorticity magnitude) is found to decrease in inverse proportion to the number of control points N, which is consistent with the vorticity error estimate stated above. Because the iteration converges so quickly, it requires a fairly modest proportion of the total computational time. For instance, in tests with 2000–4000 elements, the amplitude iteration typically requires 10–20 % of the total time, most of the rest being used for determination of the velocity field. If some degree of grouping of nearby elements were employed, such as would be done when using some type of accelerated algorithm (e.g. Greengard & Rokhlin 1987), the amplitude iteration would be significantly faster since the neighbours of each element would be known *a priori*.

Since the gradient term in (5) does not directly affect the determination of the velocity field in (2), neither does this term directly affect the vorticity solution from (1) (since ω is directly evolved on the control points). Indeed, the only effect of this term is in determination of the element amplitudes in the iteration (17). An alternative approach is to simply drop this term, by setting the matrix A_{mn} in (17) equal to zero, and to specify the values of vorticity at the control points such that the representation (6) is initially nearly divergence-free. The numerical algorithm can be shown to conserve the divergence of vorticity through first order in time step Δt during the subsequent evolution of the flow. In sample runs performed with this alternative approach, we have found that the divergence of the vorticity representation remains small during the computation provided that it is initially small and that the flow remains well resolved. Comparisons of numerous identical calculations using both the divergence and divergence-free representations give nearly identical results, even when the divergence of the vorticity representation is not small in the former case.

The Lagrangian vorticity collocation method presented here has all of the advantages usually associated with more standard vortex methods. In particular, in contrast to finite-difference or pseudo-spectral solutions of the velocity–pressure formulation of the Euler equations, Lagrangian vorticity-based methods require control points only in the portion of the flow in which a non-neglible vorticity exists (which is typically a small part of the flow field). This feature is particularly advantageous in unbounded flows, which must always be truncated to a finite domain in methods based on the velocity–pressure formulation. Secondly, Lagrangian methods do not exhibit the artificial viscosity introduced in treatments of the advection term on fixed grids. Thirdly, since we directly obtain the vorticity with error of order E_ω, say, the error in the resultant velocity after integration of vorticity in (2) is of order $E_v = O(RE_\omega)$, where R is the typical element radius. If L is a typical lengthscale of the flow geometry, then the ratio of velocity error to vorticity error is $E_v/LE_\omega = O(R/L) \ll 1$. The velocity error is thus much less than it would have been had we used a scheme with similar accuracy to directly solve for velocity.

3. Validation tests for the numerical method

Prior to considering the normal BVI problem, we present the results of a few preliminary calculations to validate various aspects of the numerical method which are pertinent to the problem to be considered. In the first test, we calculate the propagation velocity of a series of 'thin' vortex rings in order to examine the accuracy of the velocity calculation for a given vorticity field. The calculated propagation speeds U are compared to the analytical result of Saffman (1970),

$$\frac{\sigma U}{\Gamma} = \frac{\sigma}{4\pi R}\left[\ln\left(\frac{8R}{\sigma}\right) - 0.558\right], \tag{18}$$

for vortex rings with a Gaussian cross-section. In the calculations, the ring was formed of N elements which are placed along the axis of the vortex. The number of elements was adjusted to yield a given value of the ratio C of the element radius to the distance between neighbouring elements, called the 'overlap'. The calculated propagation speeds, shown in figure 1, for an overlap of $C \approx 3.0$ are found to be within 1 % of those predicted by (18) for $R/\sigma \geqslant 3$. For the case with $R/\sigma = 2$, the calculated and theoretical results differ by 3.5 %, although in this case the 'thin ring' assumption is not well satisfied and the theoretical result (18) would not be expected to be very accurate. In order to quantify the error in velocity prediction caused by inadequate resolution of the vorticity field, the calculated ring propagation speed is shown in figure 2 with different overlap values for a ring with $R/\sigma = 5$. The computed results yield a value of dimensionless ring propagation speed of about 0.0474 for overlap values above about 0.75; however, as the overlap value decreases below about 0.5, the computed propagation speed decreases rapidly.

A second set of tests, which examines the accuracy of the method for prediction of vortex-induced forces on immersed bodies, was performed for the problem of the induced force due to a vortex ring on a sphere. The vortex ring is located at some distance L from the centre of a sphere of radius a, and the ring is oriented such that its axis of symmetry passes through the sphere centre. This problem can be solved analytically using Helmholtz's (1858) solution for flow induced by a vortex ring together with Butler's (1953) sphere theorem. The solution is obtained in terms of elliptic integrals which are evaluated numerically; the derivation is given in Appendix A. Numerical calculations for this problem were performed using a vortex ring of ring radius $R = 1$ and core radius $\sigma = 0.1$, formed from 100 elements placed along the vortex axis with an overlap of 1.6. The sphere was simulated using 400 vortex sheet panels, using an algorithm similar to that of Hess & Smith (1967). The pressure is calculated in both the numerical and analytical cases using the steady Bernoulli equation, so that the force on the sphere does not include possible unsteady effects associated with movement of the vortex ring. A comparison of the drag coefficient, $C_D = \text{drag}/(\frac{1}{2}\rho\Gamma^2)$, for the numerical and analytical results are shown in figure 3 for values of the ratio L/a between 0 and 2.0. The difference between the calculated and theoretical results is less than 1 % for all cases considered.

A third test of the numerical algorithm was made to examine how well the algorithm approximates the stretching term in the vorticity transport equation. In this test, we consider a vortex ring which is being axisymmetrically stretched by a line source

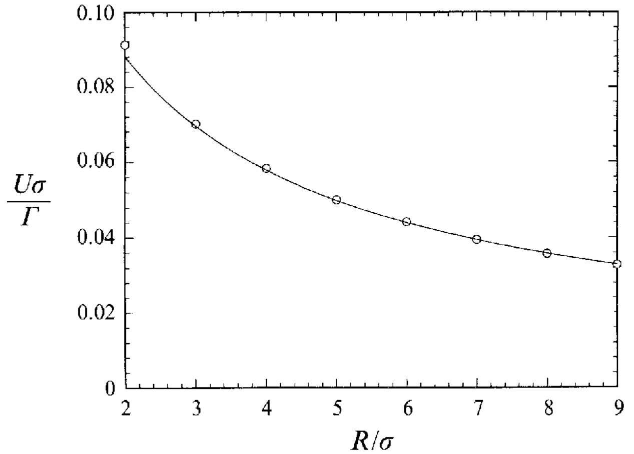

FIGURE 1. Comparison of computed (○) results for dimensionless propagation speed of a vortex ring with predicted values (solid curve) from (18), using an overlap value of 3.

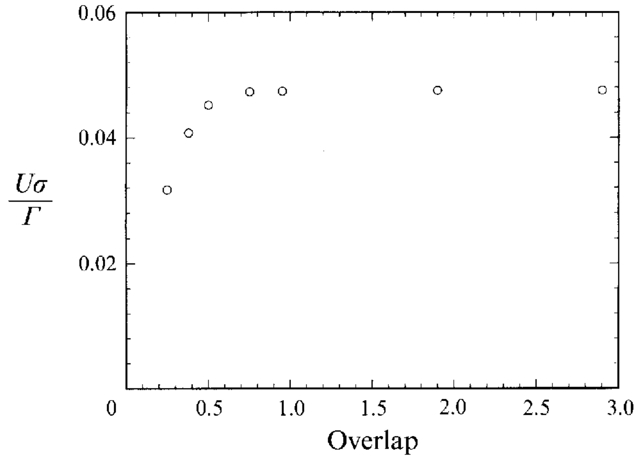

FIGURE 2. Effect of element overlap on the computed results for dimensionless propagation speed of a vortex ring with $R/\sigma = 5$.

located along the central axis of the ring. The ring is discretized by 7000 vorticity elements, which are located on 35 circular curves (with 200 control points on each curve) that form a torus. The circular curves are arranged such that a diameter of the core passes through (or close to) approximately seven control points. The vortex core is initially circular, and the vorticity distribution is initially assumed to vary in proportion to distance from the ring central axis. The length and velocity scales are non-dimensionalized by the initial core radius σ and the ratio Γ/σ of circulation to core radius, respectively. The dimensionless ring radius is initially set equal to four, and it increases to a mean value of nearly eight by the end of the computation. The computation was performed using 164 time steps, during which interval the vortex completed nearly two rotations about the core. A plot in figure 4 shows results for circulation and the ratio of average vorticity over a cross-section, ω_{ave}, to its initial value, ω_{init}, as functions of ring radius, which is defined as the distance from the ring axis to the radial centroid of the core cross-section. Dotted lines shown in the figure represent theoretical values. The circulation, which was determined by integrating the

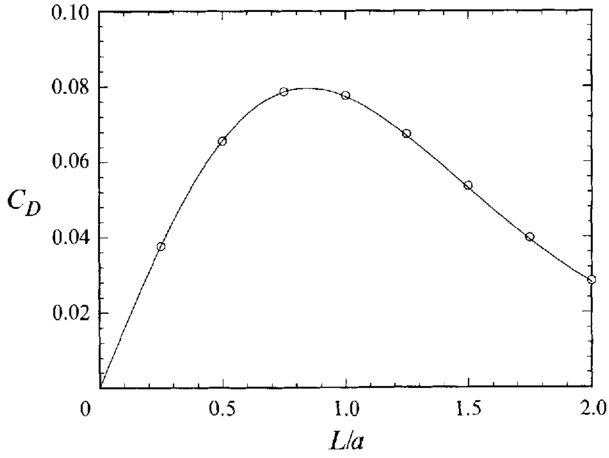

FIGURE 3. Comparison of computed (○) drag coefficient of a sphere due to velocity induced from a vortex ring, with $R/\sigma = 10$, with theoretical result (solid curve) as a function of the dimensionless distance L/a of the ring from the sphere leading edge.

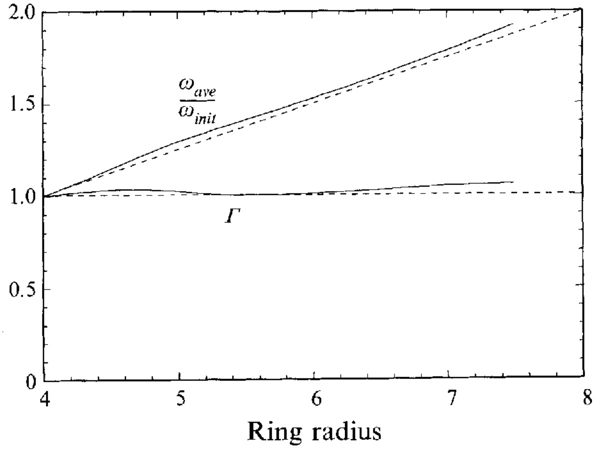

FIGURE 4. Comparison of the circulation, Γ, and the ratio of average vorticity over a cross-section to its initial value, $\omega_{ave}/\omega_{init}$, with theoretical values (dashed lines) for a vortex ring which is stretched by the flow due to a line source along the ring axis. The ring radius, defined by the distance from the ring axis to the centroid of the vortex core, approximately doubles during the course of the calculation.

tangential component of velocity over a circuit about the core, is observed to vary by a maximum of about 6% from its initial value. The computed value of $\omega_{ave}/\omega_{init}$ varies nearly linearly with ring radius, as predicted by inviscid theory. This test indicates that gross properties of the vorticity field are accurately predicted by the collocation algorithm even though the spacing between control points grows increasingly anisotropic with time.

4. Numerical implementation for the normal BVI problem

This section describes the set-up and numerical implementation of the method described in §2 for calculations of the normal BVI problem. Throughout the remainder of the paper, all length variables are non-dimensionalized by the blade chord c,

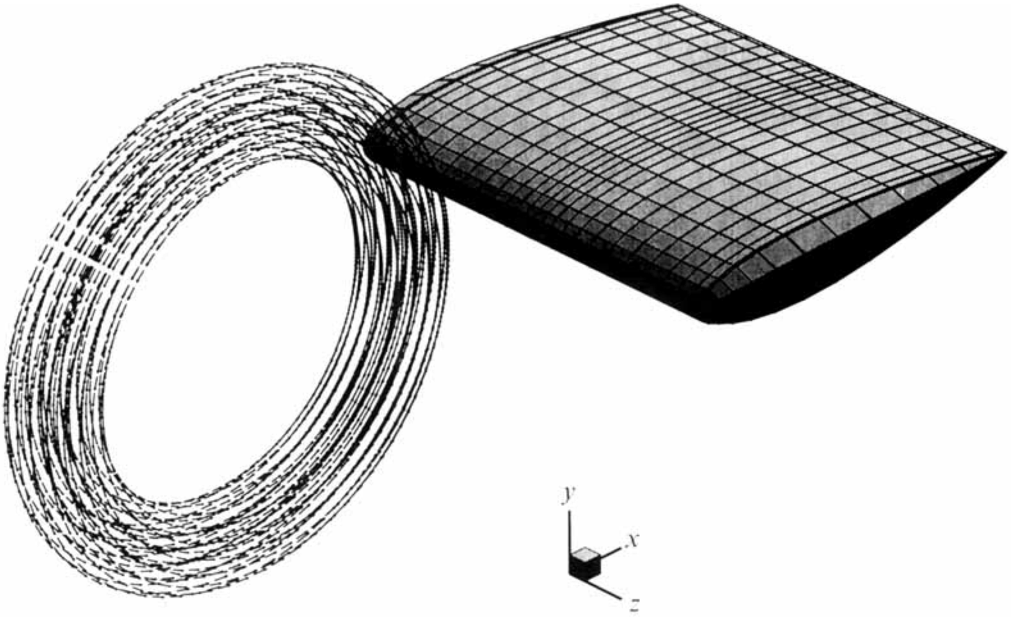

FIGURE 5. Perspective view of the initial configuration for the normal BVI computations, showing the grid lines on the blade surface and the orientation of the blade and ring with the coordinate axes. The leading edge of the blade coincides with the z-axis.

circulation is non-dimensionalized by the product Uc, where U is the free-stream velocity, and time is non-dimensionalized by c/U. In these calculations, the blade is a NACA series 0016 airfoil, with span and chord lengths equal to unity, thickness $T = 0.16$ and cosine tip shape. The vortex has the shape of a ring with ring radius $R = 0.5$ and nominal core radius $\sigma_0 = 0.1$. Three runs are reported, for values of the vortex circulation Γ of 0.2, 0.5 and 1.0. The ring is oriented such that the ring axis is parallel to the blade leading edge, as shown in figure 5, and the free stream carries the ring into the blade leading edge. A coordinate system (see figure 5) is introduced such that the z-direction is along the blade leading edge, the x-direction is along the blade chord and the y-direction is normal to the symmetry plane of the blade. The blade is stationary and its leading edge is coincident with the line $x = y = 0$. The centre of the ring is initially located at a distance of $x = -0.75$ upstream of the blade leading edge. Since the ring also propagates in the z-direction under its self-induced velocity field, an initial spanwise displacement of the ring is introduced such that the blade–vortex collision will occur close to the blade centre ($z = 0$).

The blade surface is discretized into 900 quadrilateral panels, which are placed closer together near the centre of the blade span (where the blade impacts the vortex ring) than near the tips. Calculations are performed with both moderate and high resolution of the vorticity field within the vortex ring. In the moderate resolution runs, the ring is represented by 3500 control points, which are distributed within the ring in a torus formed of 35 circular curves with 100 control points along each curve. In the high resolution runs, the ring is represented by 10500 control points, which are distributed within the ring in a torus formed of 70 circular curves with 150 control points along each curve. The circular curves are arranged in such a way that a diameter of the core would pass through (or close to) 7 control points in the moderate resolution runs and 11 control points in the high resolution runs. The vorticity distribution is initially chosen to vary linearly with radius from the ring central axis (i.e. the z-axis), such that as the elements are convected around the vortex, stretching and compression of the vortex lines allow the vorticity to remain constant at any spatial location translating with the ring. The spacing of element control points within the ring is roughly three times as close near the region where the blade impinges on the vortex ring than away from this region. A comparison between the results of the moderate and high resolution runs is given in Appendix B.

A general three-dimensional panel method was used to enforce the no-penetration condition on the blade surface. The panel solution was based primarily on a vortex sheet method (Hess & Smith 1967), where the integrals over the panels are evaluated analytically. Additional source panels were also employed since, when used alone, discretization errors in the vortex sheet method can lead to small errors in satisfaction of the no-penetration condition at the panel control points. As demonstrated by Uhlman & Grant (1993), the source sheet strength approaches zero as the number of panels increases. The Kutta condition at the trailing edge of the blade was maintained by the flow symmetry.

Time advancement of the system was performed using the second-order predictor–corrector method given in (16*a*, *b*) with a time step of 0.005. The calculations were run for 70 time steps and were stopped at time $t = 0.35$, at which point the blade has completely penetrated through the ambient position of the vortex core. For the moderate resolution cases, runs were performed in which the time step was allowed to vary during the calculations between about 0.002 and 0.0001, with no noticeable difference in the computed results.

One advantage of Lagrangian vorticity-based methods is that it is relatively easy to make the calculations self-adaptive. For instance, in the current calculations the radius of the vorticity elements was fit adaptively, by searching for nearest neighbours in three directions about each element, in order to ensure an overlap value of at least two. The nominal initial element radius size was 0.04 for the moderate resolution cases and 0.03 for the high resolution cases. The element radius decreased for control points that approached the blade surface to about 0.03–0.025 for the moderate resolution cases and about 0.015–0.008 for the high resolution cases.

In an inviscid flow with sufficiently large vortex ring radius R and blade chord and span lengths, and with no vortex axial flow or blade angle of attack, the normal blade–vortex interaction is controlled by the two dimensionless parameters T/σ_0 and $\Gamma/2\pi\sigma_0 U$. As shown in Marshall & Yalamanchili (1994), for values of T/σ_0 much greater than unity the vortex bends about the blade leading edge without penetration of the blade into the vortex core. In the present computations, the value of T/σ_0 is fixed at 1.6, which is sufficiently large for resolution of the vortex response to the blade while still in the regime that the blade penetrates the vortex core. Computations are performed for three values of the parameter $\Gamma/2\pi\sigma_0 U$: 0.32, 0.79 and 1.6. These values correspond to cases where the maximum vortex circumferential velocity is smaller than, on the same order as and somewhat greater than the uniform flow speed, respectively. All numerical results reported here were performed taking $A_{mn} = 0$ in (17), which helps speed up the iteration used to fit the element amplitudes. The run with $\Gamma/2\pi\sigma_0 U = 1.6$ was repeated allowing A_{mn} to be non-zero with nearly identical results.

Several previous studies of sound generation by normal BVI, including Howe (1989) and Amiet *et al.* (1990), have made use of rapid distortion theory (RDT) to simplify calculation of the vorticity deformation, sometimes in concert with other approximations. In RDT, the vorticity is not allowed to deform under the full velocity field, but is instead assumed to evolve with only the velocity field of the ambient potential

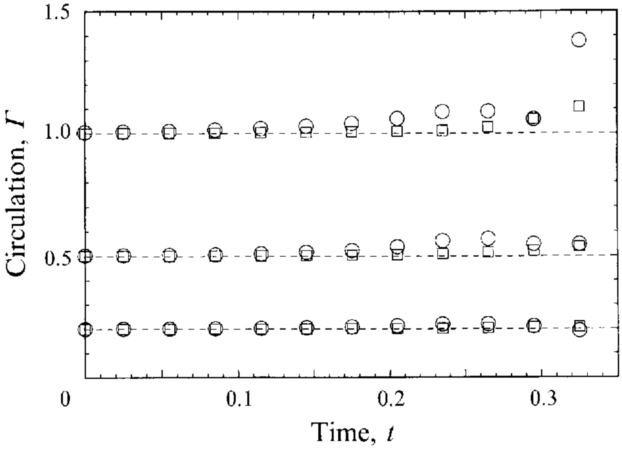

FIGURE 6. Plot of the variation with time of the computed values of circulation in the $y = 0$ plane as the vortex is penetrated by the blade for the three nominal circulation values considered (shown by a dashed line). Points denoted by squares are computed using integration of velocity over a contour about the vortex core and points denoted by circles are computed by integration of vorticity over the cross-sectional area of the core.

flow $v = U\nabla\phi$ past the blade. In order for RDT to be valid, it is necessary for the time-scale $t_d \approx T/U$ associated with deformation of the vorticity by the ambient potential flow to be small compared to the convection time $t_c \approx 2\pi\sigma_0^2/\Gamma$ of the vortex-induced motion. This condition implies that the parameter $\epsilon \equiv t_d/t_c \approx (T/\sigma_0)(\Gamma/2\pi\sigma_0 U) \ll 1$. One goal of the calculations reported in this paper is to assess the use of RDT for the normal BVI problem by comparison with results of the full inviscid calculations with different values of ϵ. The three cases considered in the paper, with $T/\sigma_0 = 1.6$ and $\Gamma/2\pi U\sigma_0 = 0.32$, 0.79 and 1.6, correspond to ϵ values of 0.5, 1.3 and 2.5, respectively.

5. Results for the deformation of the vorticity field during normal BVI

In order to evaluate the ability of the numerical method to resolve the vorticity deformation throughout the blade penetration process, the vortex circulation is calculated over a cross-section of the vortex core in the plane $y = 0$, which coincides with the plane occupied by the blade chord. The circulation calculation is performed using two different methods. In the first, the vortex-induced velocity tangent to a circuit surrounding the core, with a radius of three times the core radius, is integrated over the circuit to yield the circulation. In the second method, the vorticity is interpolated using the representation (6) onto a uniform grid on the plane $y = 0$, with 151 grid points on each side spanning the interval $(-0.5, 0.05)$ in x and $(-0.4, 0.4)$ in z, and the component of vorticity normal to this plane is integrated over area to obtain the circulation. A plot showing the results for these two methods of circulation measurement is given in figure 6 for high resolution runs with the three values of Γ considered in the paper. In this figure, square symbols denote results using the first method for circulation measurement and circular symbols denote results using the second method. The dashed lines correspond to the nominal values of circulation prescribed in the initial plane for the three cases. For all times shown, except for the last time considered for the case $\Gamma = 1$, the circulation obtained by either of these methods differs from the initial circulation by no more than 10%. In the last point shown in figure 6 for the case $\Gamma = 1$, the circulation obtained by the second method is

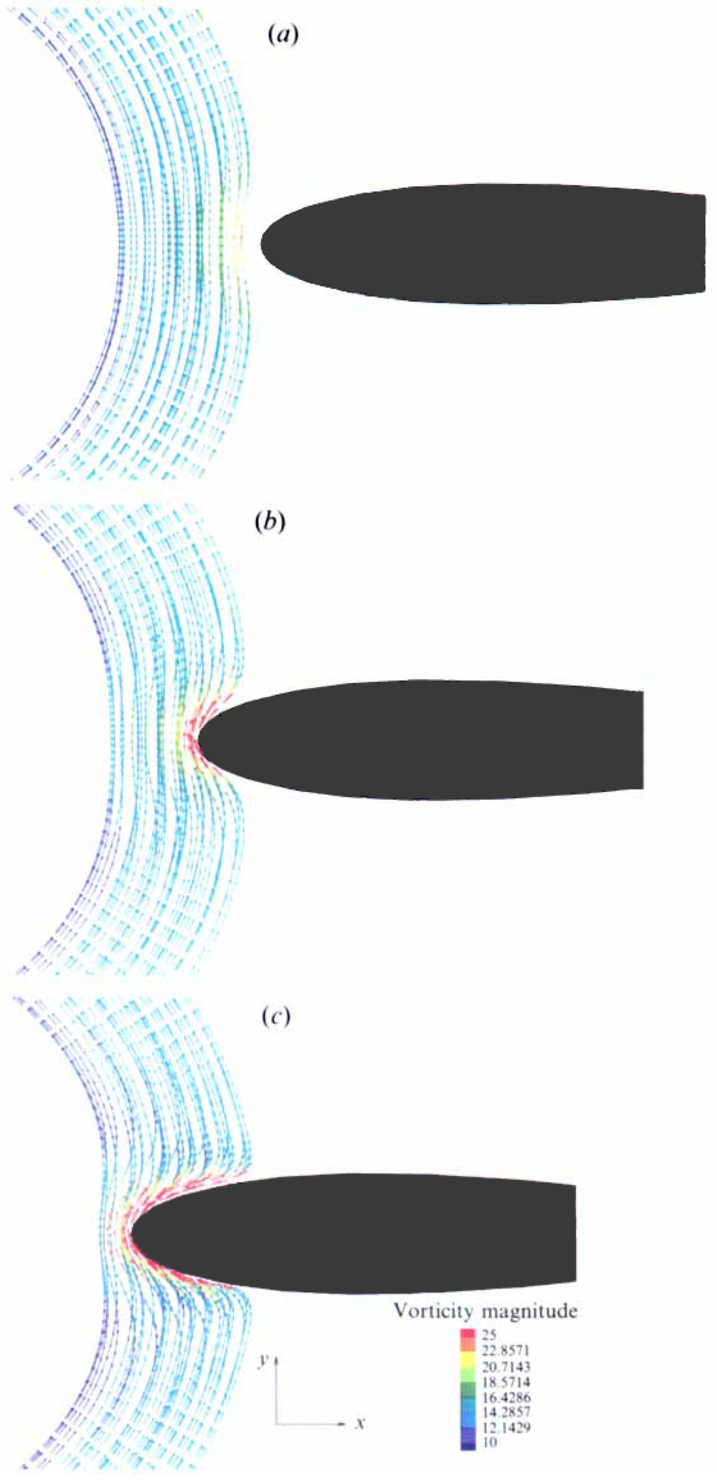

FIGURE 7. Side view of the vorticity field for the case with $\Gamma/2\pi\sigma_0 U = 1.6$. The normalized vectors indicate the direction of the vortex vector and the colour shading indicates the vorticity magnitude. Plots are drawn at times (*a*) $t = 0.154$, (*b*) $t = 0.232$ and (*c*) $t = 0.320$.

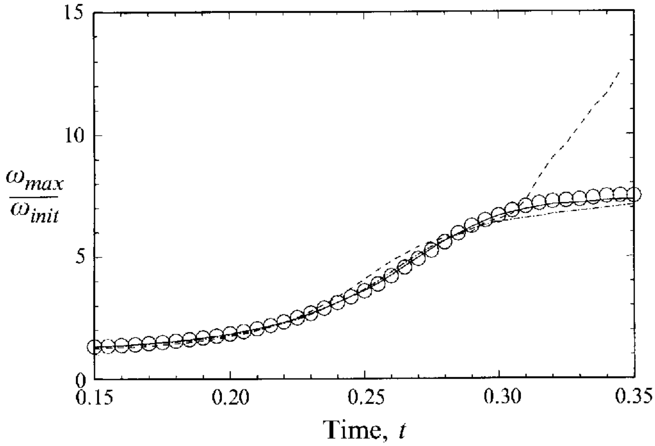

FIGURE 8. Plot of average vorticity magnitude of the 30 control points with highest vorticity magnitude for cases with strong, moderate and weak vortices, with $\Gamma/2\pi\sigma_0 U = 1.6$ (dashed curve), 0.79 (dashed–dotted curve) and 0.32 (solid curve), in comparison to RDT results (circles). The RDT results are the same for all values of $\Gamma/2\pi\sigma_0 U$.

37 % larger than the initial value, whereas that obtained by the first method is about 10 % larger than the initial value. This point occurs at a time when the penetration of the blade through the ambient position of the vortex core is 87 % complete. The differences between the two measures of circulation at this point could be indicative either of inadequacy of the resolution (6) during the later stages of the penetration (as will be discussed further presently) or of significant non-zero values of the vorticity divergence.

It is found for all three values of $\Gamma/2\pi U\sigma_0$ considered that the vortex core exhibits relatively little response as it approaches the blade, aside from a slight flattening of the core, until the point where the blade leading edge actually begins to penetrate into the vortex core. If the vortex were to be convected with the uniform flow speed alone, the blade would begin penetrating the vortex at a dimensionless time of $t = 0.15$ and penetrate entirely through the vortex by $t = 0.35$. Plots showing the vorticity field for the case $\Gamma/2\pi\sigma_0 U = 1.6$ for a moderate resolution run at dimensionless times $t = 0.154$, 0.232 and 0.320 are given in figures 7(*a*)–7(*c*), respectively, using normalized arrows to indicate the direction of the vorticity vector and colour shading to indicate the vorticity magnitude. As would be expected from Helmholtz's observation that vortex lines and material lines coincide for an inviscid fluid, the computed vortex lines deform about the blade leading edge but are not cut by the blade. The highest vorticity magnitudes are observed to occur very close to the blade surface and to form a 'ribbon' of vorticity about the surface as the vortex is convected past the blade.

The average vorticity magnitude, ω_{max}, of the 30 control points with the highest vorticity magnitudes, divided by the initial maximum vorticity magnitude ω_{init}, is plotted in figure 8 versus time for all three values of the parameter $\Gamma/2\pi\sigma_0 U$ with the high resolution runs. The time interval shown corresponds to that over which the vortex penetration occurs. The selection of 30 control points over which to average vorticity magnitude was found to give values fairly close to the peak vorticity values, while being somewhat smoother than averages with a smaller number of points. Results for the full inviscid calculations are shown by solid, dashed-dotted, and dashed curves for cases with $\Gamma/2\pi U\sigma_0 = 0.32$, 0.79 and 1.6, respectively. The results for $\omega_{max}/\omega_{init}$ obtained from the three RDT calculations were identical, since the vorticity was deformed only by the ambient potential flow. The RDT results are shown in figure 8 by circular symbols. The values of $\omega_{max}/\omega_{init}$ shown in figure 8 for the two full inviscid calculations with circulation of $\Gamma = 0.2$ and 0.5 are very close for the RDT results. In the case with $\Gamma = 1$, the value of this ratio deviates from that for the RDT calculation at a time of about 0.31, after about 80% of the blade penetration is complete. The deviation of $\omega_{max}/\omega_{init}$ for the strong vortex case from that obtained for weaker vortices could be caused by stretching of the vorticity by interaction with its image in the blade, which would not be as prevalent for cases with weaker vortices, or by the numerical difficulties encountered at the end of this run, as noted in the discussion of figure 6.

As the blade penetrates into the vortex core, the vorticity in the region near the blade leading edge is stretched about the blade and should increase at nearly an exponential rate. By contrast, the maximum vorticity values in figure 8 show a flattening off at a time of about 0.30 (after about 75% of the penetration is complete) for the RDT cases and for the full inviscid calculations with the two lower values of circulation. The maximum value that the vorticity can attain is limited by the resolution (i.e. the control point spacing) in a region very close to the blade leading edge. In the moderate resolution runs, the maximum vorticity values were found to level off somewhat earlier, as might be expected, after a time of about 0.26 (see Appendix B).

There are two shortcomings of existing vortex blob methods for computation of flows about immersed bodies, the resolution of which is a topic for additional research. The first of these has to do with the fact that even though the control points do not enter into the interior of the body, the vortex blob representation (6) used to obtain the velocity field nevertheless carries vorticity into the body interior owing to the finite size of the vorticity elements. The minimum radius of the elements is set by the restriction that sufficient element overlap be maintained tangent to the body surface, and the vorticity ribbon which wraps about the body surface can become no thinner than this minimum element radius. The extent of vorticity overhang into the blade interior in the present calculations is evidenced in the contour plot in figure 9 for the case with $\Gamma = 1$ at time $t = 0.25$. The contour plot was obtained by interpolating the vorticity field, using the representation (6), onto a regular grid on the plane $y = 0$. The grid used is the same as that described previously for the circulation calculations in figure 6. The presence of a 'ribbon' of high vorticity near the blade leading edge (indicated by a dashed line) is apparent in figure 9. It is noteworthy, however, that the vorticity is not distributed evenly in the spanwise direction, but instead has larger magnitude close to the region where the vortex circulation carries the vorticity into the blade surface (on the bottom part of the vortex in figure 9). In the present calculations, the effect of vorticity overhang into the body interior is partially countered by evaluating the surface velocity at a small distance (0.01) inside the body. A more long-range solution (towards which we are presently working) would be the development of anisotropic elements for vortex blob methods, for which the element aspect ratio and radius could be fit independently to both maintain sufficient overlap tangent to the body and reduce the vorticity overhang into the body interior to a negligible amount.

A second shortcoming of existing three-dimensional vortex methods has to do with the fact that the velocity field possesses singularities at the lines joining the vorticity panels on the body. These singularities can potentially lead to anomalous values of vortex stretching at control points coming very close to the panel edges. While panel edge singularities do not seem to have any significant effect on the computations shown in this paper, they can lead to difficulties for very high resolution runs with small values of the time step unless an effort is made to keep the points sufficiently far away from

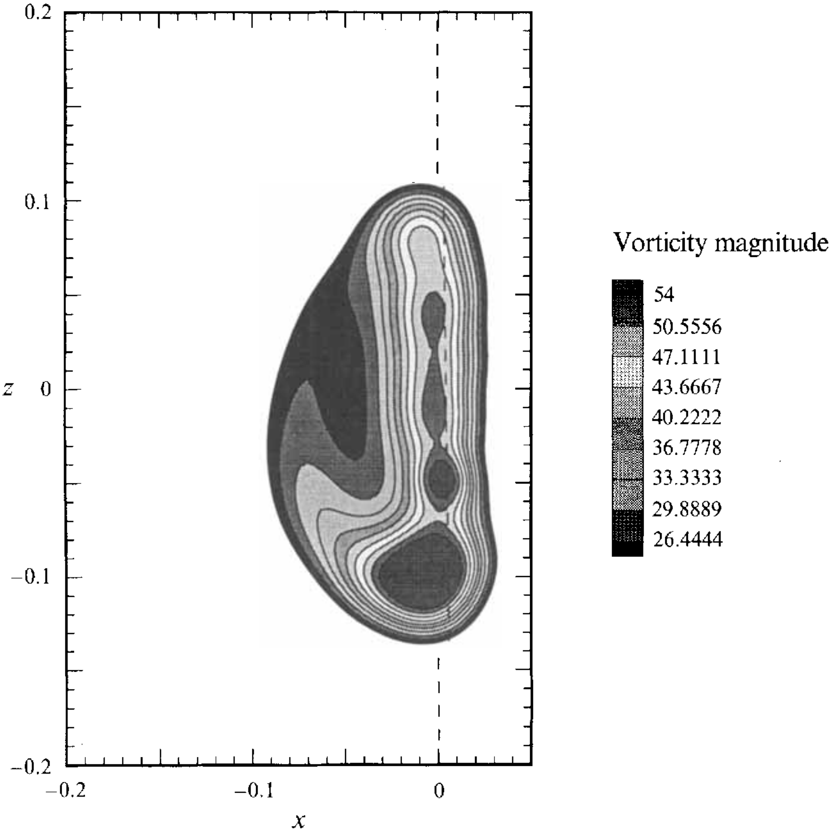

FIGURE 9. Contour plot of the vorticity magnitude on the plane $y = 0$ for the case $\Gamma/2\pi\sigma_0 U = 1.6$ at time $t = 0.25$, obtained by interpolating the vorticity onto a uniform grid using the representation (6). The dashed line indicates the position of the blade leading edge.

the panel edges. In such cases, the maximum vorticity values are observed to become very noisy and the computation quickly breaks down. The only long-range solution to this problem is to develop panels that can be joined without edge singularities.

A variety of diagnostic tests given in this section strongly support our contention that the blade penetration into the vortex core is accurately computed by our method during the first 75–80% of the penetration process (for the high resolution run). It is to be expected that any numerical method will break down at some point during the penetration, since the thickness of the vortex ribbon near the blade leading edge approaches zero exponentially at large time. In the present high resolution calculations, the results indicate that this breakdown in resolution occurs just after $t = 0.30$. This resolution limitation results in an artificial thickening of the vorticity ribbon which wraps about the blade surface, but the circulation of the vortex core near the blade leading edge is fairly well conserved. While we cannot at this time determine the exact effect of the vortex ribbon thickening during the last 20–25% of the penetration process on calculation of blade surface pressure and unsteady force, runs with different numbers of control points and different minimum element radii suggest that the effect is small (e.g. see the C_D results in Appendix B).

6. Unsteady blade surface pressure

In this section, results for the computed unsteady blade surface pressure during normal BVI are given. Since the blade surface is immersed in a non-zero vorticity field during penetration of the blade into the vortex core, the simple unsteady Bernoulli equation does not apply. We instead base our pressure calculations on an integral equation formation of the pressure-Poisson equation, which results in a Fredholm equation of the second kind for the pressure. Following Uhlman (1992), this equation for pressure is derived directly from Green's third identity, which gives the value of any scalar function ζ at a point $\boldsymbol{x}$ on the surface S of an immersed body as

$$2\pi\zeta(\boldsymbol{x}) = \int_S \zeta \frac{\partial}{\partial n}\left(\frac{1}{r}\right) \mathrm{d}a - \int_S \frac{1}{r}\frac{\partial \zeta}{\partial n} \mathrm{d}a - \int_V \frac{1}{r} \nabla^2 \zeta \, \mathrm{d}v, \tag{19}$$

where $\partial/\partial n = \boldsymbol{n}\cdot\nabla$, $\boldsymbol{n}$ is the outward unit normal of the surface S (pointing into the volume V occupied by the fluid) and, as before, $r = |\boldsymbol{x}-\boldsymbol{x}'|$. The Cauchy principal value of the integrals evaluated over S is implied. Although the function ζ may also depend on time t, time dependence is not explicitly indicated in this section.

A function B is defined by

$$B \equiv \frac{p-p_\infty}{\rho} + \tfrac{1}{2}(u^2 - U_\infty^2), \tag{20}$$

where the constants p_∞ and U_∞ are the constant pressure and velocity at infinity. The Euler equation can be written in terms of B as

$$\frac{\partial \boldsymbol{u}}{\partial t} + \nabla B - \boldsymbol{u}\times\boldsymbol{\omega} = 0. \tag{21}$$

Taking the divergence of (21) and the scalar product of (21) with $\boldsymbol{n}$ gives expressions for $\nabla^2 B$ and $\partial B/\partial n$ in an incompressible fluid as

$$\nabla^2 B = \nabla\cdot(\boldsymbol{u}\times\boldsymbol{\omega}), \quad \frac{\partial B}{\partial n} = -\boldsymbol{n}\cdot\frac{\partial \boldsymbol{u}}{\partial t} + \boldsymbol{n}\cdot(\boldsymbol{u}\times\boldsymbol{\omega}). \tag{22}$$

If we now replace the arbitrary function ζ in (19) with B and use (22), a non-homogeneous integral equation for B is obtained of the form

$$2\pi B(\boldsymbol{x}) - \int_S B \frac{\partial}{\partial n}\left(\frac{1}{r}\right) \mathrm{d}a = \int_S \frac{1}{r}\left[\boldsymbol{n}\cdot\frac{\partial \boldsymbol{u}}{\partial t} - \boldsymbol{n}\cdot(\boldsymbol{u}\times\boldsymbol{\omega})\right] \mathrm{d}a - \int_V \frac{1}{r}\nabla\cdot(\boldsymbol{u}\times\boldsymbol{\omega})\, \mathrm{d}v. \tag{23}$$

Assuming that the body is either fixed or moving steadily, the right-hand side of (23) can be reduced to a single term to obtain a Fredholm integral equation of the second kind for B as

$$2\pi B(\boldsymbol{x}) - \int_S B \frac{\boldsymbol{n}\cdot\boldsymbol{r}}{r^3} \mathrm{d}a = \int_V \frac{\boldsymbol{r}}{r^3}\cdot(\boldsymbol{u}\times\boldsymbol{\omega})\, \mathrm{d}v. \tag{24}$$

The vorticity in the region V occupied by the fluid is contained both in the interior of V and in the vortex sheet on the surface S of V. Letting the volume integral on the right-hand side of (24) be denoted by the variable J, the contribution J_{surf} due to the vortex sheet on the surface S can be written (for a stationary body) in terms of the magnitude γ of the vortex sheet strength as

$$J_{surf}(\boldsymbol{x}) = -\pi\gamma^2 + \int_S \frac{\gamma^2}{2}\frac{\boldsymbol{n}\cdot\boldsymbol{r}}{r^3} \mathrm{d}a, \tag{25}$$

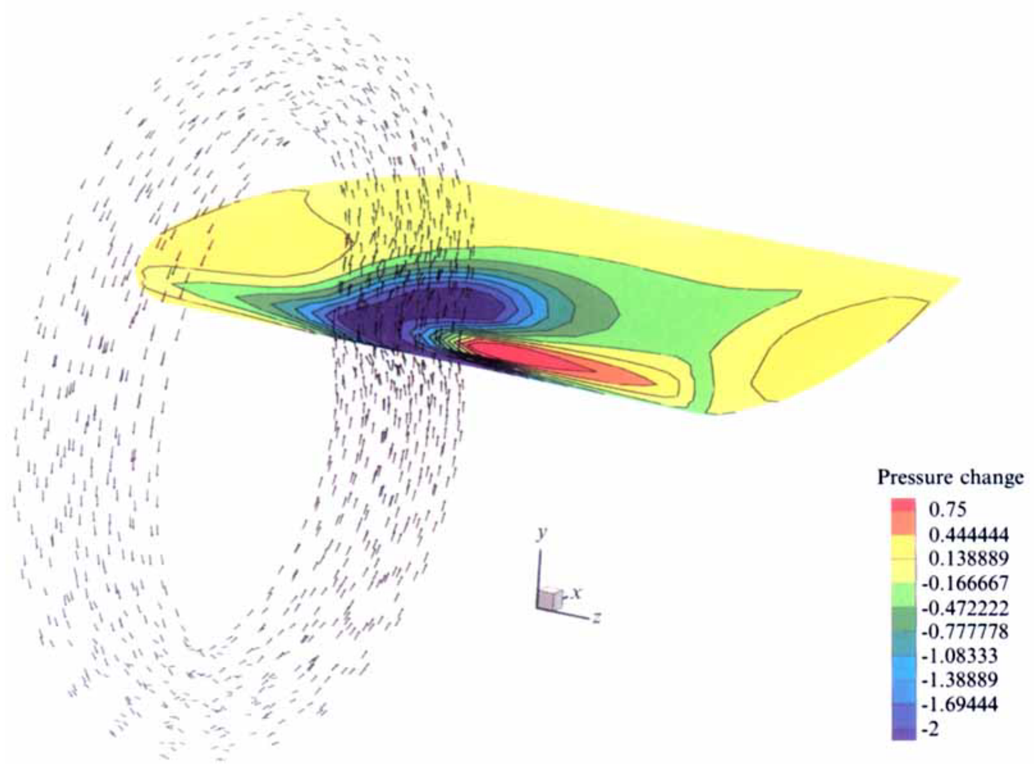

FIGURE 10. Contour plot of the pressure change on the blade surface due to the vortex for a case with $\Gamma/2\pi\sigma_0 U = 1.6$ and at time $t = 0.264$. Only one in four of the vorticity control point positions are shown to indicate the position of the vortex.

where again the Cauchy principal value of the integral is implied. Substituting (25) into (24) gives an integral equation for the quantity $B^2+(\gamma^2/2)$ as

$$2\pi\left(B+\frac{\gamma^2}{2}\right)-\int_S\left(B+\frac{\gamma^2}{2}\right)\frac{\boldsymbol{n}\cdot\boldsymbol{r}}{r^3}\,\mathrm{d}a = J_{int}, \tag{26}$$

where J_{int} denotes the part of J due to vorticity in the interior of V. For a flow which is everywhere irrotational (except on S), J_{int} would vanish and (26) would admit the solution $B+(\gamma^2/2)=0$, which is equivalent to the Bernoulli equation for steady irrotational flow.

To obtain an expression for J_{int}, we employ the algorithm described in §2 for integration of a field defined on a set of irregularly spaced points. A representation for $\boldsymbol{u}\times\boldsymbol{\omega}$ is introduced in terms of overlapping Gaussian elements, similar to that for $\boldsymbol{q}$ in (6), as

$$\boldsymbol{u}\times\boldsymbol{\omega} = \sum_{n=1}^{N} \boldsymbol{C}_n(t) f_n(\boldsymbol{x}-\boldsymbol{x}_n, R_n(t)), \tag{27}$$

where f_n is the same weighting function and $\boldsymbol{x}_n$ the same element control points as in (6). The vectors $\boldsymbol{C}_n$ can be fit to the values of $\boldsymbol{u}\times\boldsymbol{\omega}$ at the element control points using an iterative relationship similar to (17). Substituting (27) into the volume integral and performing the integration for weighting functions of the form (8) gives

$$J_{int} = \sum_{n=1}^{N} \frac{P(\frac{3}{2}, |\boldsymbol{x}-\boldsymbol{x}_n|^2/R_n^2)}{|\boldsymbol{x}-\boldsymbol{x}_n|^3}[\boldsymbol{C}_n\cdot(\boldsymbol{x}-\boldsymbol{x}_n)], \tag{28}$$

where $P(\cdot,\cdot)$ is again the incomplete gamma function.

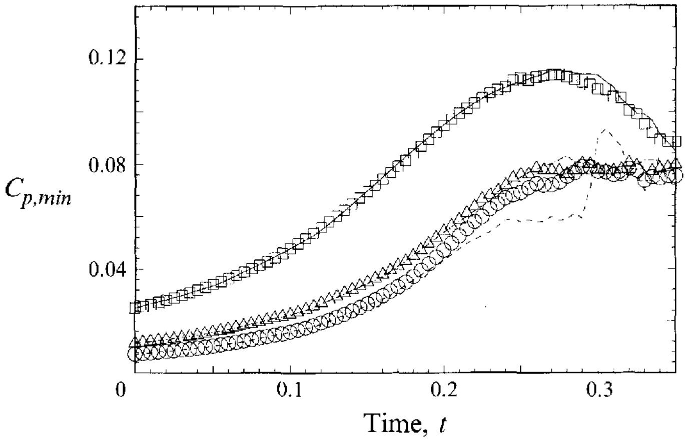

FIGURE 11. Plot of variation of the minimum value of the blade surface pressure coefficient $C_{p,min}$ with time for cases with strong, moderate and weak vortices, $\Gamma/2\pi\sigma_0 U = 1.6$ (dashed curve), 0.79 (dashed–dotted curve) and 0.32 (solid curve), in comparison to RDT results, denoted by circles, triangles and squares, respectively.

A contour plot of the change in blade surface pressure from its value without the vortex present is given in figure 10 for a moderate resolution run with $\Gamma/2\pi\sigma_0 U = 1.6$. The plot is at $t = 0.264$, at which time the vortex penetration is roughly half completed, and shows the vorticity vector only at every fourth control point in order to indicate the general location of the vortex. The pressure signature on the blade surface is dominated by a 'V' of low pressure, in the centre of which (at the blade leading edge) there is a patch of high pressure. The low-pressure patches on the top and bottom of the blade are due to the low pressure within the vortex core, and the low- and high-pressure regions along the blade leading edge are caused by the induced velocity from the vortex as it impinges on the blade. The 'waviness' of the element arrows at the top and bottom of the ring is an optical effect due to looking along the core axis (such waviness is not apparent in the side view in figure 7*b*).

The pressure signature for the weak vortex case appears similar to that shown in figure 10, except that high-pressure regions are also found on the top and bottom of the blade on the opposite side (i.e. for opposite values of z) of that on which the low-pressure regions occur. The general appearance of the pressure signature for weak vortices is that of two interlocking 'V's of high and low pressure.

A plot of time variation of the pressure coefficient $C_{p,min}$ associated with the minimum surface pressure on the blade, defined by

$$C_{p,min} = \frac{p_0 - p_{min}}{\frac{1}{2}\rho\Gamma^2/\sigma_0^2}, \tag{29}$$

is given in figure 11 for the high resolution calculations with three different values of ring circulation. Results of the full inviscid calculations are shown by continuous curves and results for RDT calculations are shown by symbols. In the implementation of RDT in our computations, the vorticity is convected with only the ambient potential flow but the full velocity is used for evaluation of pressure. It is found that if only the ambient potential flow is used in the pressure calculation, the computed unsteady drag force on the blade is much too small. In an analytical study using RDT together with the thin-airfoil approximation, Howe (1989) also found that spanwise velocity components, induced by the vortex and its image over the blade surface, play an important role in determination of the unsteady blade force.

The results of the full inviscid computations for the lower two circulation values compare closely with the RDT runs, but the results for the highest circulation value oscillate about the RDT results. The pressure field for runs with strong vortices is dominated by the vortex-induced velocity and would therefore be expected to vary approximately in proportion to Γ^2. For much weaker vortices, the pressure field is influenced more by the perturbation which the vortex causes to the ambient velocity field, and would therefore vary approximately in proportion to $U\Gamma$. Since the three cases plotted in figure 11 include vortices ranging from fairly weak to fairly strong, the minimum pressure coefficient (as defined by (29)) is lower for cases with stronger vortices.

7. Implications for modelling of unsteady blade forces

The unsteady force (drag) on the blade is calculated by integration of the change in pressure (in comparison to the ambient pressure) times the inward unit normal over the surface of the body. The computational results for vortex-induced drag D on the blade are plotted in figure 12 for high resolution runs in terms of the drag coefficient C_D, defined by

$$C_D = \frac{-D}{\frac{1}{2}\rho\Gamma^2}. \tag{30}$$

The computed results for C_D from the RDT calculations are found to be identical (to within plotting accuracy) for all three values of circulation considered, even though the pressure results shown in figure 11 are quite different. Furthermore, the results of the full inviscid calculations are found to coincide very closely with the RDT results for $t < 0.29$ for all three circulation values considered. For $t > 0.29$, the full inviscid calculations for the cases with $\Gamma = 0.5$ and 1.0 (corresponding to $\epsilon = 0.79$ and 1.6, respectively) give somewhat larger values for C_D than predicted by RDT. Since both the maximum vorticity values and the minimum pressure values for the case with $\Gamma = 0.5$ agree closely with the RDT results during this time period (as shown in figure 8 and 11), it seems unlikely that the observed differences in drag coefficient for this case are due to numerical resolution difficulties (which would tend to have most effect on points with largest vorticity values in the ribbon about the blade surface). These differences in C_D with the RDT predictions seem to arise from breakdown of the RDT assumption as the parameter ϵ approaches and exceeds unity, resulting in differences in large-scale deformation of the vortex between the RDT and full inviscid calculations.

The variation of blade penetration force with Γ^2, which is evident from figure 12 during the first 70–75% of the penetration process, can be explained by recalling the identity obtained by Howe (1989, equation (A 4)), which gives the drag force due to an inviscid vorticity field external to a stationary body, with constant uniform flow at infinity, by the integral

$$D = \rho \int_V \nabla\phi \cdot (\boldsymbol{\omega} \times \boldsymbol{u}_{vort})\, \mathrm{d}v. \tag{31}$$

Here ϕ is the velocity potential due to a uniform potential flow (with unity flow speed at infinity) past the body and $\boldsymbol{u}_{vort}$ is the velocity induced by the vortex and its image. If the deformation of the vorticity field were due primarily to the ambient potential flow past the body, as assumed in RDT, then both $\boldsymbol{\omega}$ and $\boldsymbol{u}_{vort}$ would be proportional to Γ, so that D would be proportional to Γ^2 and (31) would yield the result that the value of C_D is independent of Γ (as our computed results with RDT show). On the other hand, if the vortex were sufficiently strong that the vortex-induced or image

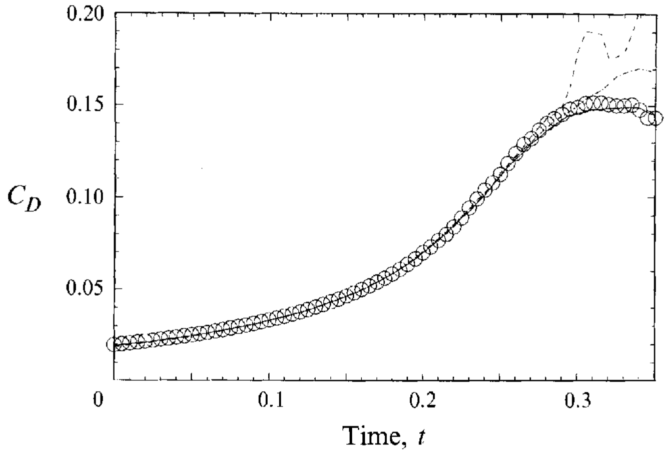

FIGURE 12. Plot of variation of the drag coefficient C_D with time for cases with strong, moderate and weak vortices, $\Gamma/2\pi\sigma_0 v = 1.6$ (dashed curve), 0.79 (dashed–dotted curve) and 0.32 (solid curve), in comparison with RDT results (circles). The RDT results are the same for all values of $\Gamma/2\pi\sigma_0 U$.

velocity contributed significantly to deformation of the vorticity field, then the vortex stretching term in (1) would exhibit terms which are both linear and quadratic in Γ, and (31) would indicate that the drag will no longer be proportional to Γ^2.

It may be of interest at this point to compare the magnitude of the blade penetration force with that of other forces present in typical normal BVI applications. For instance, in most practical applications where a vortex is cut by a blade, there is some non-zero ambient axial flow within the vortex which leads to a difference in vortex core radius across the blade surface after cutting (as noted in several of the experimental studies cited in § 1). This difference in core radius over the blade surface leads to a normal force F on the blade, derived in Marshall (1994), with magnitude

$$F \approx \frac{\rho \Gamma^2}{4\pi} \ln(\sigma^+/\sigma^-), \tag{32}$$

where σ^+ and σ^- are the vortex core radii above and below the blade, respectively. For sufficiently large axial flow (on the order of the vortex swirl velocity), equation (35) of Marshall (1994) can be used to approximate the logarithmic term in (32), giving the peak unsteady force magnitude due to the axial flow as

$$F \approx \frac{\rho \Gamma^2}{\pi}\left(\frac{2\pi\sigma_0 w_0}{\Gamma}\right)^2. \tag{33}$$

Assuming a value of axial flow speed of about one-third of the maximum vortex swirl velocity (which is typical for certain rotocraft applications), the expression (33) gives unsteady force predictions which are of the same order of magnitude as the peak values shown in figure 12. For cases with very small values of T/σ_0, the force due to vortex axial velocity would dominate the blade penetration force.

For non-zero angles of attack α, the normal BVI force is calculated in Marshall & Yalamanchili (1994) prior to impact of the blade on the vortex using a vortex filament model. This force is found to increase with increasing values of α and T/σ_0. For instance, in figure 10 of Marshall & Yalamanchili (which is for a case with $T/\sigma_0 = 5$ and attack angles of $\alpha = 0°$ and $15°$), the peak drag coefficients are found to be about $C_D = 0.3$ and 0.5, respectively. In comparison, if we assume that the blade penetration force increases in proportion to the ratio T/σ_0 (for sufficiently small values of this ratio) and vanishes for $T/\sigma_0 = 0$ (both of which are consistent with the result in equation (3.20) of Howe 1989), the peak value from figure 12 can be extrapolated for a case with $T/\sigma_0 = 5$ to give a peak value of $C_D \approx 0.5$. Thus for $T/\sigma_0 = O(1)$, the blade penetration force makes a significant contribution to the total vortex-induced force on the blade in most practical situations.

8. Conclusions

In this paper, a Lagrangian vorticity-based computational method is described and applied to the problem of penetration of a blade into a vortex core. The computational method is based on a collocation solution of the vorticity transport equation over a set of convected control points. A representation of the vorticity field in terms of overlapping elements, with one element centred at each control point, is used to obtain the velocity field at any point in the flow once the element amplitudes are known. The element amplitudes are in turn obtained from the vorticity at the N element control points by an iterative solution of an $N \times N$ matrix equation. The computational method was found to perform very well in a variety of test calculations.

Simulations using this computational method for the problem of penetration of a blade into a vortex core in an inviscid fluid indicate that the vorticity field agglomerates into a thin vortex 'ribbon' near the blade leading edge. The computational method performed well in maintaining connectedness of the vortex lines and conserving vortex circulation provided that a sufficient number of control points are used. Some difficulties were encountered owing to limitations of the computations in resolving the very thin vortex ribbon on the blade surface during the last 20–25 % of the penetration process.

The blade surface pressure is obtained by solution of a Fredholm integral equation of the second kind over the blade surface. The vortex exerts a suction force on the blade which is found to vary in proportion to the square of the vortex circulation. The computed results for unsteady blade force are found to compare well with the results of an approximate computation using rapid distortion theory, which supports use of this approximation in previous analyses of sound generation in normal BVI by Amiet *et al.* (1990), Simonich, Amiet & Schlinker (1990) and Howe (1989). The resulting values of unsteady force due to blade penetration into the vortex core are found to be of a similar order of magnitude to other forces in typical normal BVI problems for cases with $T/\sigma_0 = O(1)$.

The research reported in this paper suggests the need for additional research on a variety of topics. The use of three-dimensional vortex methods for flow past immersed bodies would be greatly facilitated by development of smooth anisotropic vorticity elements and vorticity panels on the body surface which can be joined without edge singularities. Further research is also required for the problem of normal blade–vortex interaction to clarify the final stages of the penetration process, as well as a variety of problems related to the role of viscosity (such as decay of the vortex ribbon and joining of the vortex lines in the vortex to those in the blade boundary layer).

The authors would like to express appreciation for many invaluable discussions with Dr J. S. Uhlman on the formulation of the numerical method, the assistance of Mr Hongbo Chen in producing the graphics, and helpful suggestions made by the referees of the paper. The work of J.S.M. was supported by the US Army Research Office through grant number DAAH04-93-G-0378 with The University of Iowa and by the ASEE/Navy Summer Faculty Research Program during the summer of 1993. The work of J.R.G. was supported by the US Office of Naval Research under grant number N0001493WX22029 and by internal funding from the Naval Undersea Warfare Center, Division Newport.

Appendix A. Analytical solution for vortex ring–sphere problem

This Appendix gives the derivation of the analytical solution for interaction between a vortex ring and a sphere, which is used in §3 to compare with the results of the Lagrangian vorticity computations. We recall the standard solution for the streamfunction ψ_0 due to an isolated vortex ring of circulation Γ,

$$\psi_0(\rho, z) = \frac{\Gamma(R\rho)^{1/2}}{2\pi}\left[\left(\frac{2}{k}-k\right)K(k)-\frac{2}{k}E(k)\right], \tag{A 1}$$

where ρ and z are the radial and axial coordinates of a cylindrical polar coordinate system, R is the ring radius and $K(k)$ and $E(k)$ are the complete elliptic integrals of the first and second kinds. For a ring with centre located at $(\rho, z) = (0, z_0)$, the constant k is given by

$$k^2 = \frac{4R\rho}{(z-z_0)^2+(R+\rho)^2}. \tag{A 2}$$

A sphere of radius a can be introduced at the origin O of the (ρ, z) coordinate system with use of Butler's (1953) sphere theorem for axisymmetric flows, which gives the streamfunction ψ for the sphere–ring problem as

$$\psi(r, \theta) = \psi_0(r, \theta)-\frac{r}{a}\psi_0\left(\frac{a^2}{r}, \theta\right), \tag{A 3}$$

where spherical coordinates (r, θ) are related to the polar coordinates (ρ, z) by

$$\rho = r\sin\theta, \quad z = r\cos\theta. \tag{A 4}$$

The velocity components v_r and v_θ are given by

$$v_r = \frac{1}{r^2\sin\theta}\frac{\partial\psi}{\partial\theta}, \quad v_\theta = -\frac{1}{r\sin\theta}\frac{\partial\psi}{\partial r}. \tag{A 5}$$

Substituting (A 1) and (A 2) into (A 3) and evaluating the result on the sphere surface $r = a$, v_θ becomes

$$v_\theta\bigg|_{r=a} = -\frac{\Gamma}{\pi}\left(\frac{R}{a\sin\theta}\right)^{1/2}\frac{\mathrm{d}k}{\mathrm{d}r}\left\{\left[-\frac{2}{k^2}-1\right]K(k)+\frac{2}{k^2}E(k)+\left[\frac{2}{k}-k\right]\frac{\mathrm{d}K(k)}{\mathrm{d}k}-\frac{2}{k}\frac{\mathrm{d}E(k)}{\mathrm{d}k}\right\}, \tag{A 6}$$

where derivatives of the elliptic integrals are given by (Gradshteyn & Ryzhik 1980, p. 907)

$$\frac{\mathrm{d}K(k)}{\mathrm{d}k} = \frac{E(k)}{kk'^2}-\frac{K(k)}{k}, \quad \frac{\mathrm{d}E(k)}{\mathrm{d}k} = \frac{E(k)-K(k)}{k} \tag{A 7}$$

and $k' \equiv (1-k^2)^{1/2}$. The derivative $\mathrm{d}k/\mathrm{d}r$ in (A 6) can be obtained simply by substituting (A 4) into (A 2) and differentiating with respect to r. The elliptic integrals in (A 6) were computed using the algorithm provided by Press *et al.* (1992).

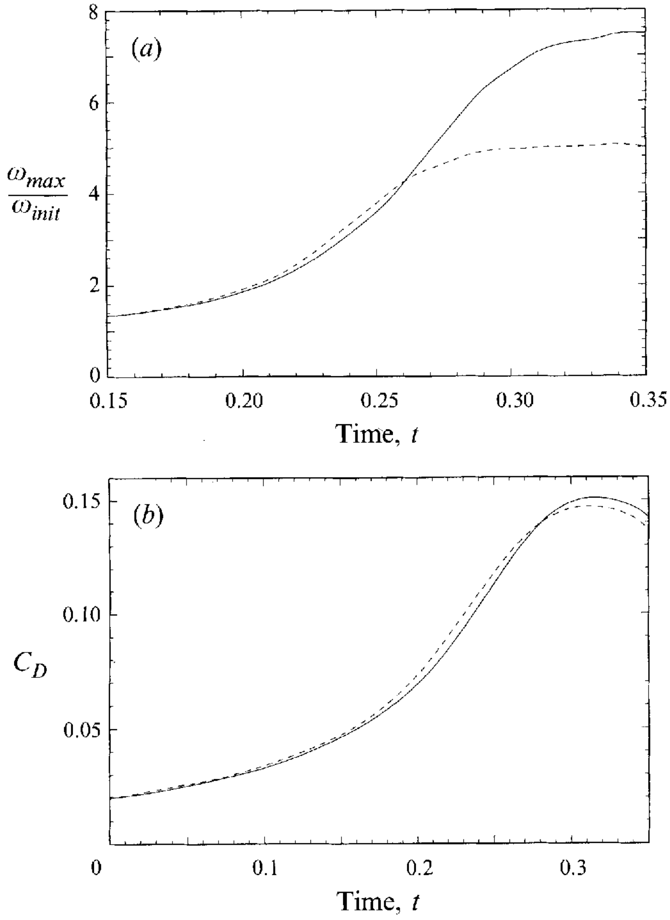

FIGURE 13. Plots comparing values of (*a*) the ratio $\omega_{ave}/\omega_{init}$ and (*b*) the drag coefficient C_D obtained from RDT calculations with moderate resolution (dashed line) and high resolution (solid line) runs. The high resolution results (with 10500 points) were obtained by averaging over the 30 strongest points, while the moderate resolution results (with 3500 points) were obtained by averaging over the strongest 10 points.

Appendix B. Comparison of results for moderate and high resolution runs

The results of RDT calculations performed using moderate and high resolution are compared in this Appendix to assess the effect of vorticity resolution on the computational results. In making such a comparison, it is important to consider the effect of the finite element size on the effective radius of the vortex core. In the calculations used for this comparison with both high and moderate resolution runs, the maximum element radius was set equal to 0.03 and the outermost control points in the core were placed at a distance of 90 % of the core radius from the centre. The effective core radius, calculated based on the maximum vorticity magnitude in the core at the initial time step, was found to be 0.113 for the high resolution runs and 0.115 for the moderate resolution runs, for a case with a nominal core radius of $\sigma_0 = 0.1$. The circulation of the core was equal to the nominal value 0.500 in both cases to within four significant figures at the initial time and was conserved to within 3 % during the calculations.

Results of RDT calculations for the high and moderate resolution calculations are shown in figure 13. In figure 13(*a*), the vorticity ratio $\omega_{ave}/\omega_{init}$ is plotted during the penetration of the blade into the vortex core. To account for the difference in number of control points, the maximum vorticity magnitude was obtained by averaging over the 30 strongest points for the high resolution runs and averaging over the 10 strongest points for the moderate resolution runs. The vorticity ratio results for the two calculations are initially close, but moderate resolution results flatten out sooner and to a lower value of $\omega_{ave}/\omega_{init}$ than the high resolution results, as would be expected from the discussion in §5. The minimum element radius in the high resolution runs reduces from 0.03 to about 0.015 for points near the blade surface during the penetration, whereas for the moderate resolution runs the element radius remains at 0.03 for all elements. The results, both for vorticity magnitude and element radius, indicate that the limiting thickness of the high-vorticity ribbon about the blade surface for the moderate resolution runs is between about 1.5 to 2 times the thickness for the high resolution runs near the end of the penetration process.

Despite the considerable difference in the resolution of the near-surface vorticity, the drag coefficient results for the high and moderate resolution runs, shown in figure 13(*b*), are extremely close throughout the entire calculation (with a difference of no more than 3%). These data thus support our claim that the thickness of the vorticity ribbon about the blade surface has very little effect on the calculation of drag on the body.

Another, less empirical, way of arriving at the same conclusion follows from Howe's identity (31). Since the three vectors $\nabla\phi$, $\boldsymbol{\omega}$ and $\boldsymbol{u}_{vort}$ are all co-planar at the blade surface, the integrand of (31) will vanish for vorticity on the blade surface. This suggests that the high-vorticity ribbon wrapped about the blade surface may have only a secondary role in determination of the force on the body, as originally suggested by Howe (1989). Of course, the velocity induced by near-surface vorticity is still important when evaluating $\boldsymbol{u}_{vort}$ in (31) at points located farther from the surface (which make the most significant contribution to this integral), but these points are sufficiently distant from the surface that only the strength (and not the thickness) of the vorticity ribbon will be significant in determination of the induced velocity. One advantage of Lagrangian vorticity-based methods, as opposed to Eulerian methods using primitive variables, is that circulation is approximately conserved even when the flow is not particularly well resolved.

REFERENCES

Abramowitz, M. & Stegun, I. A. 1965 *Handbook of Mathematical Functions*. Dover.

Ahmadi, A. R. 1986 An experimental investigation of blade-vortex interaction at normal incidence. *J. Aircraft* **23**, 47–55.

Amiet, R. K. 1986 Airfoil gust response and the sound produced by airfoil-vortex interaction. *J. Sound Vib.* **107**, 487–506.

Amiet, R. K., Simonich, J. C. & Schlinker, R. H. 1990 Rotor noise due to atmospheric turbulence ingestion. Part II. Aeroacoustic results. *J. Aircraft* **27**, 15–22.

Anderson, C. & Greengard, C. 1985 On vortex methods. *SIAM J. Numer. Anal.* **22**, 413–440.

Beale, J. T. 1986 On the accuracy of vortex methods. In *Proc. Workshop on Comput. Fluid Dyn. & Reacting Gas Flows, IMA, University of Minnesota.*

Beale, J. T. & Majda, A. 1982 Vortex methods. Part I. Convergence in three dimensions. *Math. Comput.* **39**, 1–27.

Beck, J. V., Blackwell, B. & St. Clair, C. R. 1985 *Inverse Heat Conduction*. John Wiley & Sons.

Butler, S. F. J. 1953 A note on Stoke's stream function for motion with a spherical boundary. *Proc. Camb. Phil. Soc.* **49**, 169–174.

Cary, C. M. 1987 An experimental investigation of the chopping of helicopter main rotor tip vortices by the tail rotor. Part II. High speed photographic study. *NASA CR*-177457.

CHOQUIN, J. P. & LUCQUIN-DESREUX, B. 1988 Accuracy of a deterministic particle method for Navier-Stokes equations. *Intl J. Numer. Meth. Fluids* **8**, 1439–1458.

GRADSHTEYN, I. S. & RYZHIK, I. M. 1980 *Tables of Integral, Series and Products*, Academic.

GREENGARD, L. & ROKHLIN, V. 1987 A fast algorithm for particle simulations. *J. Comput. Phys.* **73**, 325–348.

HELMHOLTZ, H. 1858 Uber Integrale der hydrodynamischen Gleichungen welche den Wirbelbewegungen entsprechen. *Crelles J.* **55**, 25.

HESS, J. & SMITH, A. 1967 Calculation of potential flows about arbitrary bodies. *Prog. Aeronaut. Sci.* **8**, 1–138.

HOWE, M. S. 1988 Contributions to the theory of sound production by vortex-airfoil interaction, with application to vortices with finite axial velocity defect. *Proc. R. Soc. Lond.* A **420**, 157–182.

HOWE, M. S. 1989 On unsteady surface forces, and sound produced by the normal chopping of a rectilinear vortex. *J. Fluid Mech.* **206**, 131–153.

JOHNSTON, R. T. & SULLIVAN, J. P. 1992 Unsteady wing surface pressures in the wake of a propellor. *AIAA Paper* 92-0277.

KNIO, O. M. & GHONIEM, A. F. 1990 Numerical study of a three-dimensional vortex method. *J. Comput. Phys.* **86**, 75–106.

KRISHNAMOORTHY, S. 1993 An experimental study of vortex response during cutting by a blade or cylinder. MS thesis, Florida Atlantic University, Boca Raton, Florida.

KRISHNAMOORTHY, S. & MARSHALL, J. S. 1994 An experimental investigation of 'vortex shocks'. *Phys. Fluids* **6**, 3737–3741.

LEONARD, A. 1985 Computing three-dimensional incompressible flows with vortex elements. *Ann. Rev. Fluid Mech.* **17**, 523–559.

LEVERTON, J. W., POLLARD, J. S. & WILLS, C. R. 1977 Main rotor wake/tail rotor interaction. *Vertica* **1**, 213–221.

LUNDGREN, T. S. & ASHURST, W. T. 1989 Area-varying waves on curved vortex tubes with application to vortex breakdown. *J. Fluid Mech.* **200**, 283–307.

MARSHALL, J. S. 1991 A general theory of curved vortices with circular cross-section and variable core radius. *J. Fluid Mech.* **229**, 311–338.

MARSHALL, J. S. 1994 Vortex cutting by a blade. Part I. General theory and a simple solution. *AIAA J.* **32**, 1145–1150.

MARSHALL, J. S. & GRANT, J. R. 1994 Evolution and breakup of vortex rings in straining and shearing flows. *J. Fluid Mech.* **273**, 285–312.

MARSHALL, J. S. & YALAMANCHILI, R. 1994 Vortex cutting by a blade. Part II. Computations of the vortex response. *AIAA J.* **32**, 1428–1436.

NOVIKOV, E. A. 1983 Generalized dynamics of three-dimensional vortical singularities (vortons). *Sov. Phys. JETP* **57**, 566–569.

PRESS, W. H., FLANNERY, B. P., TEUKOLSKY, S. A. & VETTERLING, W. T. 1992 *Numerical Recipes*, 2nd edn. Cambridge University Press.

SAFFMAN, P. G. 1970 The velocity of viscous vortex rings. *Stud. Appl. Maths* **49**, 371–380.

SCHLINKER, R. H. & AMIET, R. K. 1983 Rotor-vortex interaction noise. *AIAA Paper* 83-0720.

SIMONICH, J. C., AMIET, R. K. & SCHLINKER, R. H. 1990 Rotor noise due to atmospheric turbulence ingestion. Part 1: Fluid mechanics. *J. Aircraft* **27**, 7–14.

UHLMAN, J. S. 1992 An integral equation formation of the equations of motion of an incompressible fluid. *Naval Undersea Warfare Center, Division Newport, Tech. Rep.* 10086.

UHLMAN, J. S. & GRANT, J. R. 1993 A new method for implementation of boundary conditions in the discrete vortex element method. *Proc. ASME Fluids Engng Conf., June, Washington, DC.*

WEIGAND, A. 1993 The response of a vortex ring to a transient, spatial cut. PhD Dissertation, University of California, San Diego.

WINCKELMANS, G. S. & LEONARD, A. 1993 Contributions to vortex particle methods for the computation of three-dimensional incompressible unsteady flows. *J. Comput. Phys.* **109**, 247–273.